Rare Metal Materials and Engineering
Volume 49, Issue 9, September 2020
Available online at www.rmme.ac.cn

Science Press

Cite this article as: Rare Metal Materials and Engineering, 2020, 49(9): 2937-2947.

ARTICLE

Effect of CMAS on Interfacial Crack and Residual Stress of Thermal Barrier Coatings

Guo Dun, Yu Qingmin, Cen Lv

Northwestern Polytechnical University, Xi'an 710129, China

Abstract: With the increase of operating temperature of aero-engine turbine blades, a vitreous material (CMAS) consisting mainly of CaO, MgO, Al_2O_3 and SiO_2 are increasingly harmful to the thermal barrier coatings deposited on the blade. Therefore, the performance and durability of thermal barrier coatings should be improved. The influence of CMAS penetration on interfacial crack propagation and residual stress in the thermal barrier coatings prepared by electron beam physical vapor deposition was investigated by the finite element method. The sinusoidal curves with fixed wavelength and varying amplitude were used to model the interfaces with different roughness. At the same time, the effect of the elastic modulus of CMAS and the interaction between interface and CMAS were taken into account. The results show that the increase of CMAS elastic modulus has an inhibitory effect on interfacial cracks, and that the smaller the thermally grown oxide (TGO) amplitude and thickness, the more obvious the inhibition. There is a critical point for CMAS elastic modulus to affect the maximum residual stress S_{22} in top coat (TC) layer. Before the critical point, the change of CMAS elastic modulus has a greater influence on the maximum residual stress of TC layer, and with the increase of elastic modulus of CMAS, the maximum residual stress of TC layer decreases greatly; after the critical point, the maximum residual stress of TC layer is hardly affected by the change of elastic modulus of CMAS. These results are of great significance to study the failure mechanism of thermal barrier coatings prepared by electron beam physical vapor deposition, and can provide guidance for the optimization of the interface of thermal barrier coatings.

Key words: thermal barrier coatings; CMAS; interface morphology; interfacial crack; finite element method

Thermal barrier coatings (TBCs) are currently widely used for insulation and protection of critical metal components in the hot-side components of gas turbines, to improve the thermal efficiency of the engine by reducing the service temperature of the alloy matrix. TBCs are a multi-layer system, usually composed of substrate (SUB), bond coat (BC) and ceramic top coat (TC). When the coating works at high temperature, elements such as Al in the bonding layer will diffuse outward and oxidize, forming a thermally grown oxide (TGO) layer between the TC layer and the BC layer[1]. At present, the methods for preparing TBCs are mainly atmospheric plasma spraying (APS) and electron beam physical vapor deposition (EB-PVD). EB-PVD TBCs have a good columnar crystal structure, and their thermal shock resistance and spallation resistance are much better than those of APS coating. Therefore, EB-PVD TBCs are required for hot-side components operated in harsh environments, such as aero-engine blades[2, 3].

In the past decade, a great deal of research has been done on the durability of TBCs, mainly focusing on oxidation, erosion and foreign object damage. However, with the increase of service temperature of aero-engine, the performance and durability of TBCs have higher requirements, and further, in the coating system subjected to high temperatures, new degradation phenomena appears. In fact, under working conditions, the engine can inhale various particles (dust, sand, volcanic ash, etc.), most of which are calcium, magnesium, aluminum silicates, known as CMAS (the main chemical constituents are CaO, MgO, Al_2O_3 and SiO_2), and they are more and more harmful to the TBCs of engine blades. With

Received date: September 06, 2019
Foundation item: National Natural Science Foundation of China (11872308); Natural Science Basic Research Plan in Shaanxi Province of China (2019JM-461)
Corresponding author: Yu Qingmin, Ph. D., Professor, School of Mechanics, Civil Engineering and Architecture, Northwestern Polytechnical University, Xi'an 710129, P. R. China, Tel: 0086-29-88431000, E-mail: qingminyu@nwpu.edu.cn

the increase of operating temperature, the local surface temperature of TBCs can be higher than the melting point of CMAS[3]. Due to the excellent wettability and low viscosity of CMAS, these pollutants can penetrate into the internal pores of TBCs. It has been proved that the most successful and widely used thermal barrier coating ceramic materials, (6%~8%)Y_2O_3 partially stabilized ZrO_2 (YSZ), cannot resist CMAS corrosion. In particular, the large columnar crystal gap in typical columnar crystal structure of EB-PVD coating provides natural conditions for CMAS infiltration. Studies have shown that the CMAS deposited on the surface of the turbine blade will melt and penetrate into the YSZ when the temperature exceeds 1150 °C. When the temperature decreases, the melted CMAS will solidify between the YSZ gaps. Because of the difference of elastic modulus and thermal expansion coefficient, the strain tolerance of YSZ and interfacial bonding force will be greatly reduced, resulting in the peeling of the thermal barrier coatings from the edge of the blade or the overall peeling from the interface, eventually leading to the failure of the coating[4]. Since the erosion of CMAS mainly occurs at the high temperature stage, it inevitably costs a lot to analyze the failure process of coatings through experiments, and it is also difficult to accurately characterize the distribution of the internal stress field of the coating failure caused by CMAS during the high temperature process. In order to solve this problem, in recent years, many scholars have analyzed the influence of CMAS infiltration on coating spall by finite element method, and achieved remarkable results.

Li et al[5] investigated the thermodynamic and thermochemical interaction between the coating and molten CMAS in the early failure of TBCs, and found that porous TBCs are very susceptible to corrosion by molten CMAS. Guo et al[6, 7] studied the thermal shock life and failure mode of EB-PVD TBCs under the coupled action of CMAS and high temperature gas thermal shock. The results show that the thermal shock life of EB-PVD TBCs decreases by 60%~70% under the coupled action of CMAS.

Krämer et al[8] studied the thermochemical effect of CMAS and the evolution of morphology and structure of columnar crystal in EB-PVD ceramic layer. It was found that both the penetration and the corrosion effect of CMAS on YSZ layer are related to the initial position of transverse crack and the position at which the spallation occurs. Mercer et al[9] experimentally investigated the infiltration process of molten CMAS into columnar TC layer and the damage of the coating caused by the infiltration. They concluded that the coating is debonded and peels off when the infiltration depth of CMAS reaches a critical value. Su[10] proposed a physical model combining CMAS penetration and EB-PVD columnar microstructure. Theoretical and numerical analyses show that the CMAS penetration mainly affects the overall in-plane modulus of coatings. The mechanism of CMAS induced interfacial delamination is that CMAS penetrates into the columnar gap and increases the overall effective modulus of the surface layer, promoting the delamination of coatings. Su et al [11] further adopted the method of finite element analysis to study the effect of CMAS erosion on the delamination crack in EB-PVD TBCs with bending interfaces. The results show that it mainly occurs in the region above the curved interface, and the tensile stress level of the delamination crack decreases with the increase of the in-plane modulus of TC. At the same time, the shear stress increases, mainly appearing in the peripheral region of the bending zone. When the delamination crack extends to the region, the shear stress drives the delamination crack.

During the use of gas turbine engines, TBCs can undergo a variety of degradation mechanisms. However, these problems are mostly studied independently in laboratory, and many mechanisms usually occur at the same time in reality. People have done a lot of work on the oxidation of the BC [12-15], the interface morphology of the BC[16], the erosion of the TC[17, 18], the corrosion of the TC[19-21] and the role of material parameters of each layer causing the failure of the TBCs [22-24].

However, most of them do not consider the oxidation of BC and the influence of different interface morphologies when studying the erosion and corrosion of TC. In this study, the sinusoidal curve was used to model the interface between layers based on EB-PVD TBCs microstructure and CMAS infiltration model (Fig.1). The influence of CMAS infiltration on the propagation of BC-TGO interface cracks and residual stress was studied by finite element method. By studying the interaction between CMAS erosion and coating interface morphology, the failure mode of TBCs under CMAS erosion can be explained more comprehensively, which can provide reference for the improvement of thermal barrier coatings.

1 Finite Element Model

1.1 Geometrical model

Based on the microstructure of EB-PVD coatings (Fig.1) and CMAS infiltration characteristics, a two-dimensional plane strain model was established using commercial finite element software ABAQUS[25]. The whole model is shown in

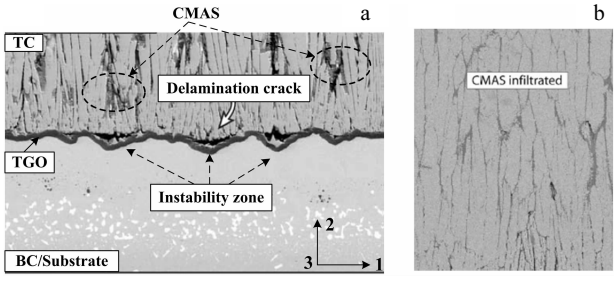

Fig.1 Micrograph of EB-PVD TBCs (a) and CMAS penetration structure (b)[11]

Fig.2. The TBCs structure consists of four layers: TC, TGO, BC and SUB. The TC consists of columnar crystal microstructures and infiltrated CMAS. It is assumed that all the columns are vertical to the interface and distributed in parallel, the spacing between the columns is d=1 μm, and the width of the column is D=9 μm. Assuming that the layers are perfectly bonded without relative sliding, and cohesive elements are embedded at the interface between TGO and BC. The thickness of each layer is h_{TC}=100 μm, h_{TGO}=5 μm, h_{BC}=100 μm and h_{SUB}=2500 μm. According to Ref.[26], the infiltration time of CMAS in the columnar crystal space is less than 1 min under the high-temperature corrosion environment of 1100 °C. So in this study, it is assumed that the CMAS is completely penetrated, namely, the penetration height of CAMS is h_{CMAS}=h_{TC}. The penetration width is the same as the columnar crystal spacing. It should be pointed out that in the actual penetration process of CMAS, a thin layer of CMAS will be deposited on the coating surface. When the molten CMAS penetrates into a region where the temperature is lower than its melting point, it will become a dense solid and stop downward penetration. CMAS partial infiltration destroys the loose structure of the coating, and divides the columnar crystal gap into two parts, namely permeated part and non-permeated one. The difference between the material parameters of the two parts will easily deduce large tensile stress due to the temperature gradient during thermal cycle. When the stress reaches the material yield limit, it will cause not only the interface crack, but also in-plane crack. This complicates the study of the fracture problems within TC layer, which will be studied further in the future. In order to simplify the analysis, the surface layer of CMAS is neglected. The interface between layers is expressed by a sine curve $y = A\sin(2\pi x/\lambda)$ to represent different roughness of interface; the wavelength λ was fixed at 60 μm, and the amplitude A was selected as 10, 15, and 20 μm.

1.2 Material parameters

In this study, the TC, TGO, substrate and CMAS were considered as elastic materials, and the BC was considered as elastic plastic material. The von Mises yield criterion was used to determine whether the stress reaches the yield strength. The material parameters involved in this study were temperature dependent. The Young's modulus and the Poisson's ratio of each layer are shown in Table 1 and Table 2, respectively; the physical parameters related to CMAS are listed in Table 3, the thermal expansion coefficient of each layer is shown in Table 4, and the yield strength of BC is shown in Table 5.

1.3 Load and boundary conditions

As shown in Fig.3, the displacement in the x direction on the left boundary, and the displacement in the y direction on the bottom boundary are fixed. A multi-point constraint (MPC) is applied on the right boundary to ensure that the right surface of model keeps a vertical plane during calculation. The TBC system is assumed to be in a uniform temperature field, so there is no thermal conduction and thermal convection between the layers. The temperature decreases linearly from the initial temperature 1100 °C to room

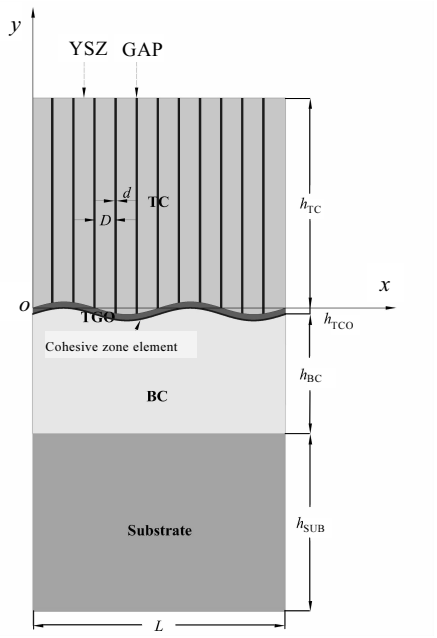

Fig.2 Schematic of two-dimensional plan strain model based on ABAQUS

Table 1 Young's modulus of each layer (GPa) [23, 27]

Temperature/°C	SUB	BC	TGO	TC
20	220	200	400	48
200	210	190	390	47
400	190	175	380	44
600	170	160	370	40
800	155	145	355	34
1000	130	120	325	26
1100	120	110	320	22

Table 2 Poisson's ratio of each layer

Temperature/°C	SUB	BC	TGO	TC
20	0.31	0.30	0.23	0.10
200	0.32	0.30	0.23	0.10
400	0.33	0.31	0.24	0.10
600	0.33	0.31	0.24	0.11
800	0.34	0.32	0.25	0.11
1000	0.35	0.33	0.25	0.12
1100	0.35	0.33	0.25	0.12

Table 3 Relevant physical parameters of CMAS[28]

Temperature/°C	Elastic modulus/GPa	Liner expansion coefficient/$\times10^{-6}$ °C^{-1}	Poisson's ratio
25		4.7	0.25
600	55	5.5	0.25
1100		6.7	0.25

Table 4 Thermal expansion coefficient of each layer ($\times10^{-6}$ °C^{-1})

Temperature/°C	SUB	BC	TGO	TC
20	14.8	13.6	8.0	9.0
200	15.2	14.2	8.2	9.2
400	15.6	14.6	8.4	9.6
600	16.2	15.2	8.7	10.1
800	16.9	16.1	9.0	10.8
1000	17.5	17.2	9.3	11.7
1100	18.0	17.6	9.6	12.2

Table 5 Yield strength of the BC (MPa)[29]

Temperature/°C	Yield strength
20	426
200	412
400	396
600	362
800	284
1000	202
1100	114

temperature (20 °C) in 120 s during calculation. The TBC system is in a stress-free state at 1100 °C. In the finite element analysis of the thermal barrier coatings, an initial stress-free state temperature was assumed. At this temperature, there is no residual stress inside the coatings. This temperature is related to the process of the coatings. And the life of coating can be improved by appropriately increasing the preparation temperature during the preparation of the coating. Therefore, the system is in a stress-free state usually at high temperatures.

The cohesive layer was meshed using four-node two-dimensional cohesive element (COH2D4), and other parts were meshed using four-node plane strain quadrilateral element with reduced integration and hourglass control (CPE4R). The entire model consists of 10 000~20 000 elements. The meshes near cohesive elements and TGO were refined. The minimum element size was 0.2 μm.

2 Interface Cohesive Model

Material failure is a rather complex process, especially for laminates or composite materials, such as the TBC system studied in this study. In recent decades, the development of various numerical methods has made it possible to simulate the formation and propagation of cracks. In this section, the cohesive model in ABAQUS software is used to simulate the failure behavior of TBCs. The cohesive model considers that the failure behavior is a process of cohesive regions at the crack tip along with the force of the material itself to resist the failure [30, 31]. In the finite element model, the cohesive region is not a real physical material, but a kind of adhesion of the material itself to the destructive behavior, and its essence is a fracture constitutive model. Therefore, the cohesive model expresses the complex fracture process by the relative separation displacement-force relationship between the two surfaces. In the analysis, cohesive elements are usually embedded between solid elements to achieve crack initiation and propagation. When fracture occurs, cracks will form and propagate along the direction of cohesive element arrangement. This simulates the failure behavior of the material. Initial thickness of cohesive element is usually set to zero, that is, cohesive element will not affect the results in calculation[32].

The cohesive model consists of six parameters: interfacial tensile strength σ_{n}^{0} and interfacial shear strength σ_{s}^{0}, critical open displacement δ_{n}^{0} and critical shear displacement δ_{s}^{0}, as well as normal fracture energy G_{n}^{0} and tangential fracture energy G_{s}^{0} (area enclosed by the cohesive model). As shown in Fig.4, the bilinear traction-separation law [33] is used to define the failure behavior of TC materials in this study. This rule uses the tensile force as a function of the separation distance, to represent the constitutive equation of the cohesive model.

The bilinear traction-separation law is expressed as below:

$$\sigma_i=\begin{cases}\boldsymbol{Z}\delta_i & \delta_i\le\delta_i^0\\ (1-N_i)K\delta_i & \delta_i^0<\delta_i<\delta_i^{\mathrm{f}}(i=\mathrm{n,s})\\ 0 & \delta_i\ge\delta_i^{\mathrm{f}}\end{cases}\tag{1}$$

$$N_i=\begin{cases}0 & \delta_i\le\delta_i^0\\ \dfrac{\delta_i^{\mathrm{f}}(\delta_i-\delta_i^0)}{\delta_i(\delta_i^{\mathrm{f}}-\delta_i^0)} & \delta_i^0<\delta_i<\delta_i^{\mathrm{f}}(i=\mathrm{n,s})\\ 1 & \delta_i\ge\delta_i^{\mathrm{f}}\end{cases}\tag{2}$$

where σ is the stress, δ is the displacement, N is the damage variable and Z is the initial interface stiffness. The superscript 0 refers to the critical displacement at the initial damage, and the superscript f refers to the displacement when the unit fails completely. The critical and tangential critical fracture energy can be expressed as follows:

$$G_{\mathrm{n}}^{\mathrm{c}}=\frac{1}{2}\sigma_{\mathrm{n}}^{0}\delta_{\mathrm{n}}^{\mathrm{f}}\tag{3}$$

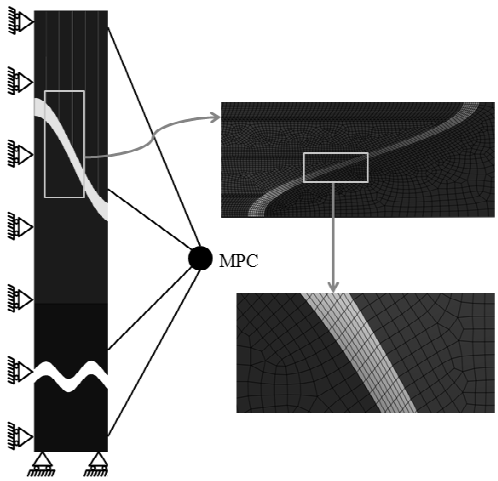

Fig.3 Boundary conditions and finite element mesh of model

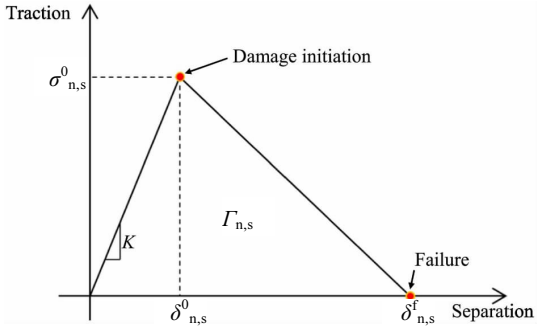

Fig.4 Bilinear traction-separation law[34]

$$G_s^c = \frac{1}{2}\sigma_s^0 \delta_s^f \tag{4}$$

Secondary normal stress criterion is chosen to describe the initial failure criterion of coatings, which is expressed as follows[35, 36]:

$$\left\{\frac{\langle\sigma_n\rangle}{\sigma_n^o}\right\}^2 + \left\{\frac{\langle\sigma_s\rangle}{\sigma_s^o}\right\}^2 = 1 \tag{5}$$

where σ_n represents the normal stress in the stretching process, σ_n^0 indicates the maximum normal stress that the material can bear; σ_s is the shear stress in the stretching process, σ_s^0 the maximum shear stress that the material can bear; < > indicates that no damage will occur under pure compression, i.e.

$$\langle\sigma_n\rangle = \begin{cases} \sigma_n & \sigma_n \geq 0 \\ 0 & \sigma_n < 0 \end{cases} \tag{6}$$

Therefore, the cohesive element will not be damaged under pure compressive stress. The evolution of damage is illustrated by the power expression[37]:

$$\left(\frac{G_n}{G_n^c}\right)^\alpha + \left(\frac{G_s}{G_s^c}\right)^\alpha = 1 \tag{7}$$

where G_n and G_s are the work done by the force in the normal and tangential directions, respectively; G_n^c and G_s^c are the critical fracture energy in both directions. Here, the power exponent α is chosen to be 1, and the total energy of crack propagation is the sum of work done by the force in the normal and tangential directions:

$$G = G_n + G_s \tag{8}$$

It should be noted that, σ_n^0 and σ_s^0, also known as cohesive strength, approximately equal to the fracture strength of the coating.

The interfacial tensile strength $\sigma_n^0 = 200$ MPa and shear strength $\sigma_s^0 = 100$ MPa. The critical fracture energy is $G_n^c = 20$ J/m^2 and the tangential critical fracture energy is $G_s^c = 60$ J/m^2. According to the relationship between stiffness and elastic modulus of materials, the stiffness is calculated as: $K_n = K_t = 10^8$ MPa/mm [38-40].

3 Results and Discussion

The effect of CMAS penetration is mainly reflected in the change of macro-modulus of TBCs. Considering the relative content of each component of the CMAS mixture and the actual change of the modulus, it is assumed that the CMAS elastic modulus ranges from 5 GPa to 120 GPa [11]. The amplitudes of TGO are taken as 5, 10, 15, and 20 μm, and the thickness of TGO is taken as 1, 3, and 5 μm. In order to express the problem more clearly, the relevant parameters in the text are dimensionless, and the dimensionless expressions of quantities are as follows:

Dimensionless crack length:

$$\bar{a} = a/L \tag{9}$$

Dimensionless elastic modulus of CMAS:

$$\bar{E} = E_{CMAS}/E_{TC}^0 \tag{10}$$

where a is the true length of the crack, L is half wavelength of the interface, and E_{TC}^0 is the elastic modulus of TC at 20 °C.

3.1 Effect of CMAS elastic modulus on BC-TGO interface crack propagation

Firstly, the influence of CMAS elastic modulus on BC-TGO interface cracks under different TGO amplitudes and thicknesses is analyzed.

Fig.5 shows the influence of CMAS elastic modulus on BC-TGO interface crack propagation under different amplitudes and thicknesses of TGO. As can be seen that, in the case of the same TGO amplitude, the BC-TGO interfacial cracks under different TGO thicknesses are gradually shortened as the elastic modulus of CMAS increases.

Fig.5a shows the effect of CMAS elastic modulus on BC-TGO interface cracks under different TGO thicknesses when the TGO amplitude is 20 μm. It can be found that the crack length when a TGO thickness is 5 μm is about 1.5 times larger than the crack length when the TGO thickness is 1 μm under the same CMAS elastic modulus. That is, for the same elastic modulus, the smaller the TGO thickness, the shorter the interface cracks. For the same TGO thickness, with increasing the elastic modulus of CMAS, the crack at BC-TGO

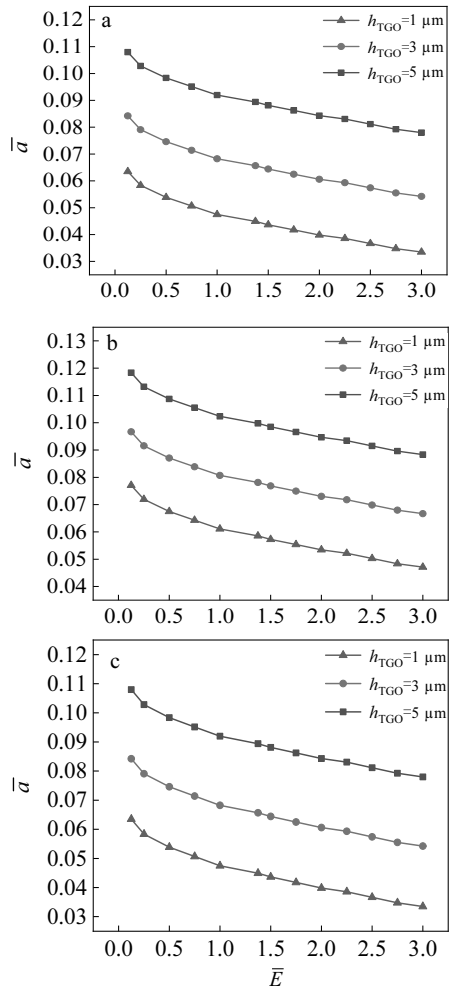

Fig.5 Effect of CMAS elastic modulus on BC-TGO interface crack propagation under different amplitudes (A) and thicknesses (h_{TGO}) of TGO: (a) A=20 μm, (b) A=15 μm, and (c) A=10 μm

interface becomes shorter. The difference is that the interfacial crack length decreases to different degrees when TGO is different in thickness. For example, as the $\bar{E}$ increases to 3, the interfacial crack length decreases by about 24% for TGO with a thickness of 5 μm, while for TGO with thickness of 1 μm, the interfacial crack length decreases by about 35%. That is to say, when the elastic modulus of CMAS increases, the smaller the thickness of TGO, the more significant the change of interfacial crack.

Fig.5b shows the effect of CMAS elastic modulus on BC-TGO interface cracks under different TGO thicknesses when the TGO amplitude is 15 μm. For the same CMAS elastic modulus, the crack length at the TGO thickness of 5 μm is about 1.7 times larger than the crack length when the TGO thickness is 1 μm, that is, the smaller the TGO thickness, the shorter the interface crack. This is the same as the conclusion obtained when the TGO amplitude is 20 μm. The BC-TGO interface crack becomes shorter as the elastic modulus of CMAS increases under the same TGO thickness. The difference is that the interfacial crack length decreases to various degrees for different thicknesses of TGO. For example, when the $\bar{E}$ increases to 3, the interfacial crack length decreases by about 25% for h_{TGO}=5 μm, while for h_{TGO}=1 μm, the interfacial crack length decreases by about 39%. That is to say, as the CMAS elastic modulus increases, the smaller the thickness of TGO, the more pronounced the change in interfacial crack.

Fig.5c shows the effect of CMAS elastic modulus on BC-TGO interface cracks for different TGO thicknesses when the TGO amplitude is 10 μm. The similar change trend to Fig.5a and Fig.5b can be found, and the difference is that the magnitude of the change is different.

As for the same CMAS elastic modulus, the crack length for a TGO thickness of 5 μm is about twice larger than that at a TGO thickness of 1 μm. When the $\bar{E}$ increases to 3, the interfacial crack length at TGO thickness of 5 μm decreases by about 28%, while that decreases by about 47% at TGO thickness of 1 μm. It can also be explained that when the elastic modulus of CMAS increases, the smaller the thickness of TGO, the more significant the change of interfacial crack.

Fig.6 shows the effect of CMAS elastic modulus on BC-TGO interface cracks at different TGO amplitudes when the thickness of TGO is 5, 3 and 1 μm. It can be seen that the BC-TGO interface cracks gradually shorten with the increase of CMAS elastic modulus under the same thickness of TGO.

Fig.6a shows the effect of CMAS elastic modulus on BC-TGO interface cracks under different TGO amplitudes when the thickness of TGO is 5 μm. It can be found that when $\bar{E}=0.125$, the normalized crack length $\bar{a}$ is approximately 0.123 for the amplitude of TGO of 20 μm, and 0.108 for the amplitude of TGO of 10 μm. The latter is about 12% lower than the former. When $\bar{E}=3$, the normalized crack length $\bar{a}$ is about 0.09 for the amplitude of TGO of 20 μm, and about 0.07 for the amplitude of TGO of 10 μm. The latter is about 16% lower than the former. That is to say, for the same thickness of TGO, the larger the TGO amplitude, the longer the interface crack length. When the CMAS elastic modulus increases, the change of the interfacial crack length caused by the change of the TGO amplitude becomes more apparent. That is, the larger the elastic modulus of CMAS, the greater the influence of the change of TGO amplitude on the interface crack length. When the $\bar{E}$ increases from 0.125 to 3, the interfacial crack length decreases by about 24% for TGO with amplitude of 20 μm, and that is 28% for TGO with amplitude of 10 μm. The results show that when the elastic modulus of CMAS increases gradually, the interfacial crack length of BC-TGO decreases with different trends.

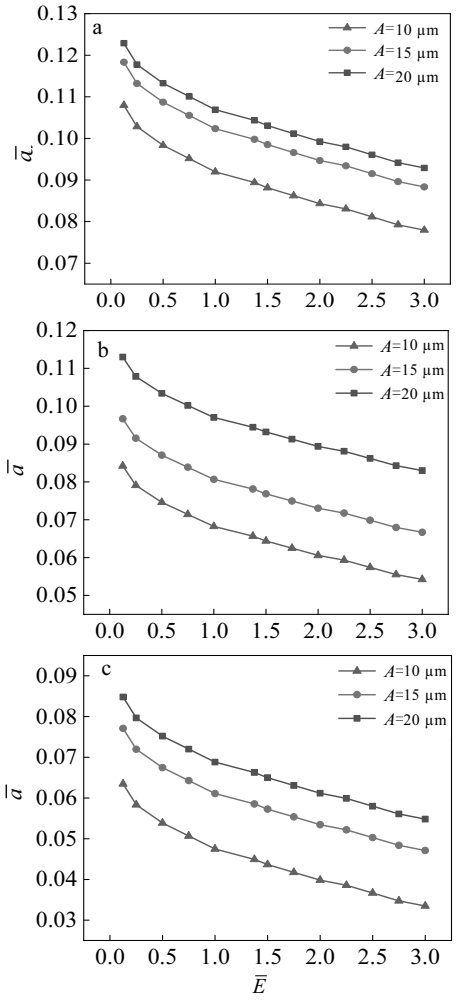

Fig.6 Effect of CMAS elastic modulus on BC-TGO interface cracks under different amplitudes (A) and thicknesses (h_{TGO}) of TGO: (a) h_{TGO}=5 μm, (b) h_{TGO}= 3 μm, and (c) h_{TGO}=1 μm

For TGO with smaller amplitude, the effect of the change of CMAS elastic modulus on the interfacial crack length is more obvious.

Fig.6b shows the effect of CMAS elastic modulus on BC-TGO interface crack propagation under different TGO amplitudes when the thickness of TGO is 3 μm. It can be found that when the elastic modulus of CMAS is 5 GPa, the normalized crack length $\bar{a}$ is about 0.113 and 0.08 for the TGO amplitude of 20 and 10 μm, respectively. The latter is about 25% lower than the former. When the elastic modulus of CMAS is 120 GPa, the normalized crack length $\bar{a}$ is about 0.08 for the TGO amplitude of 20 μm, and it is 0.05 for the TGO amplitude of 10 μm. The latter is about 35% lower than the former. This is the same as the result obtained from Fig.6a. For the same thickness of TGO, the larger the TGO amplitude, the longer the interface crack length. When the elastic modulus of CMAS increases, the change of interfacial crack length caused by the change of the amplitude of TGO becomes more obvious. That is to say, the larger the elastic modulus of CMAS, the more the interface crack length is affected by the change of TGO amplitude. When the $\bar{E}$ increases from 0.125 to 3, the decrease rate of interfacial crack length is about 26% for TGO amplitude of 20 μm, and 35% for TGO amplitude of 10 μm. The smaller the amplitude of TGO, the more obvious the interfacial crack length is affected by the change of CMAS elastic modulus.

Fig.6c shows the effect of CMAS elastic modulus on BC-TGO interface crack propagation for different TGO amplitudes when the thickness of TGO is 1 μm. When the $\bar{E}$ is 0.125, the normalized crack length $\bar{a}$ is about 0.08 for the TGO amplitude of 20 μm and 0.06 for the TGO amplitude of 10 μm. The latter is about 25% lower than the former. When the $\bar{E}$ is 3, the normalized crack length $\bar{a}$ is about 0.05 for the TGO amplitude of 20 μm and about 0.03 for the TGO amplitude of 10 μm. And the latter is about 39% lower than the former. It can be concluded that the larger the amplitude of TGO, the longer the interfacial crack length, and the greater the CMAS elastic modulus, the more the interface crack length can be affected by the change of TGO amplitude. As the $\bar{E}$ increases from 0.125 to 3, the interfacial crack length decreases by 35% for the TGO amplitude of 20 μm, and 47% for the TGO amplitude of 10 μm. That is to say, the smaller the amplitude of TGO, the greater the influence of the change of CMAS elastic modulus on the interfacial crack length.

3.2 Effect of CMAS elastic modulus on residual stress distribution in TC layer

During the service of thermal barrier coatings, the interface cracking and coat peeling are the main failure modes. The premature peeling failure of coatings will expose the alloy matrix to high temperature gas, which will lead to disastrous consequences. Previous studies have shown that the vertical stress S_{22} of thermal barrier coatings plays an important role in the cracking and spall failure of coatings[23, 41, 42]. The influence of CMAS elastic modulus on the BC-TGO interface crack propagation was analyzed systematically. And CMAS mainly exists in the columnar crystal gap of the TC layer. Therefore, in this part, the coating structure with cohesive unit shown in Fig.1 is still used. The residual stress in TC layer was investigated, considering the influence of the change of CMAS elastic modulus on structural stress under thermal load, and the variation of the amplitude and thickness of the TGO layer.

Fig.7 shows the residual stress distribution in TC layer under different CMAS elastic moduli and TGO amplitudes when the TGO thickness is 3 μm and the temperature reduces from 1100 °C to room temperature.

Fig.7a shows the residual stress distribution in TC layer under different elastic moduli of CMAS when the am-

plitude of TGO is 20 μm and thickness is 3 μm. While as the elastic modulus of CMAS increases, the maximum residual stress first decreases and then increases, and the position of the maximum residual stress also changes with the change of the elastic modulus of CMAS. When $\overline{E}$ is 0.125, the maximum residual stress is located close to the peak position. With the increase of the elastic modulus of CMAS, the maximum residual stress migrates to the center of the wave, where cracks in TC layer initiate[42]. It can be found that when the $\overline{E}$ increases from 0.125 to 3, the maximum residual stress varies greatly from 477 MPa to 311 MPa, and then increases gradually with the increase of the elastic modulus of CMAS, but the variation range is small at each time.

Fig.7b shows the residual stress distribution in TC layer with the change of elastic modulus of CMAS when the amplitude of TGO is 15 μm and thickness is 3 μm. Similar to Fig.7a, the maximum residual stress also shows a tendency to decrease first and then increase with the increase of the CMAS elastic modulus. The position of the maximum residual stress also appears near the peak position at $\overline{E}=0.125$, and the position shifts slowly to the middle of the wave with the increase of the elastic modulus of CMAS. The difference is that under the same CMAS elastic modulus, the maximum residual stress level of the TC layer with a TGO amplitude of 15 μm is relatively lower than with the TGO amplitude of 20 μm. For example, at $\overline{E}=0.125$, the residual stress is reduced from 477 MPa to 377 MPa, and at $\overline{E}=0.5$, the residual stress is reduced from 311 MPa to 240 MPa. The figure also shows the analysis of the maximum residual stress value under different CMAS elastic moduli. When $\overline{E}$ increases from 0.125 to 3, the maximum residual stress value changes greatly, and then with the increase of elastic modulus of CMAS, the maximum residual stress changes slightly.

The analysis of the residual stress distribution of the TC layer with a TGO thickness of 3 μm and amplitudes of 10 and 5 μm is the same as that of Fig.7, and the maximum residual still first decreases and then increases when the CMAS elastic modulus increases. When $\overline{E}$ increases from 0.125 to 0.5, the maximum residual stress value changes greatly. Then, with the increase of CMAS elastic modulus, the maximum residual stress value changes less.

Similarly, the position of maximum residual stress also changes with the change of the elastic modulus of CMAS. At $\overline{E}=0.125$, the maximum residual stress appears near the peak position, and its position slowly shifts to the wave as the elastic modulus of CMAS increases. The difference is that, under the same CMAS elastic modulus, compared to TGO amplitudes of 20 and 15 μm, the maximum residual stress level of the TC layer with amplitudes of 10 and 5 μm is relatively low.

Fig.8 shows the effect of CMAS elastic modulus on the maximum residual stress in TC layer at different TGO thicknesses and amplitudes. In general, with the increase of the elastic modulus of CMAS, the maximum residual stress of

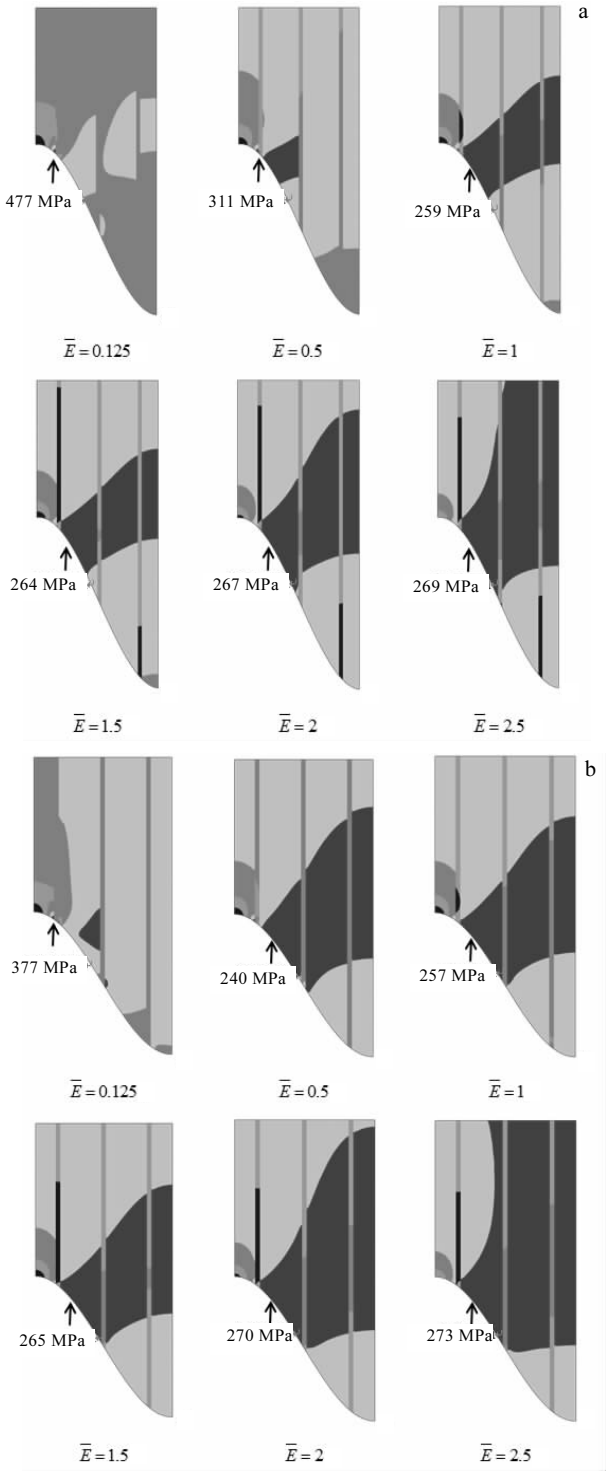

Fig.7 Residual stress distribution in TC layer under different CMAS elastic moduli and TGO amplitudes (A) with h_{TGO}=3 μm: (a) A=20 μm and (b) A=15 μm

the TC layer basically decreases first and then increases. This is the same as the conclusion obtained in Fig.7. It should be noted that under different TGO amplitudes and thicknesses, the difference in the $\overline{E}$ value corresponding to the maximum residual stress is different. For convenience of description, the $\overline{E}$, at which the trend of the maximum residual stress changes, is defined as the critical point.

Fig.8a~8d shows the curve of the maximum residual stress with the elastic modulus of CMAS when the amplitude of TGO is constant and the thickness is different. When the TGO amplitude is 5 μm (Fig.8a), the critical point of the residual stress curve under TGO thickness of 1 and 5 μm is around $\overline{E}=0.75$, and the critical point of the residual stress curve with a TGO thickness of 3 μm is around $\overline{E}=0.5$. Before the critical point, the increase of CMAS elastic modulus has obvious influence on the maximum residual stress, and the maximum residual stress decreases with the increase of CMAS elastic modulus. The curve of TGO thickness of 1 and 3 μm varies greatly, about 47% and 36%, respectively, while the curves of thickness 5 μm change slightly, about 3%.

After the critical point, the maximum residual stress of the three curves increases with the increase of CMAS elastic modulus, but the increase range is quite different. For example, the curves with TGO thicknesses of 3 and 5 μm are basically not affected by the increase of CMAS elastic modulus. While the curves of TGO thickness 1 μm increase obviously in maximum residual stress, and when CMAS elastic modulus increases to a certain value, the residual stress tends to be stable.

When the TGO amplitude is 10 μm (Fig.8b), the critical points of the three curves are all around $\overline{E}=0.5$. Before the critical point, the increase of CMAS elastic modulus has an obvious influence on the residual stress, and it decreases with the increase of CMAS elastic modulus, which is the same as the conclusion when the TGO amplitude is 5 μm. The curves of TGO thicknesses of 3 and 5 μm vary to approximately the same degree, about 20%. The curve of 1 μm varies greatly, by about 44%. After the critical point, similar to the TGO amplitude of 5 μm, the maximum residual stress of the three curves increases with the increase of the CMAS elastic

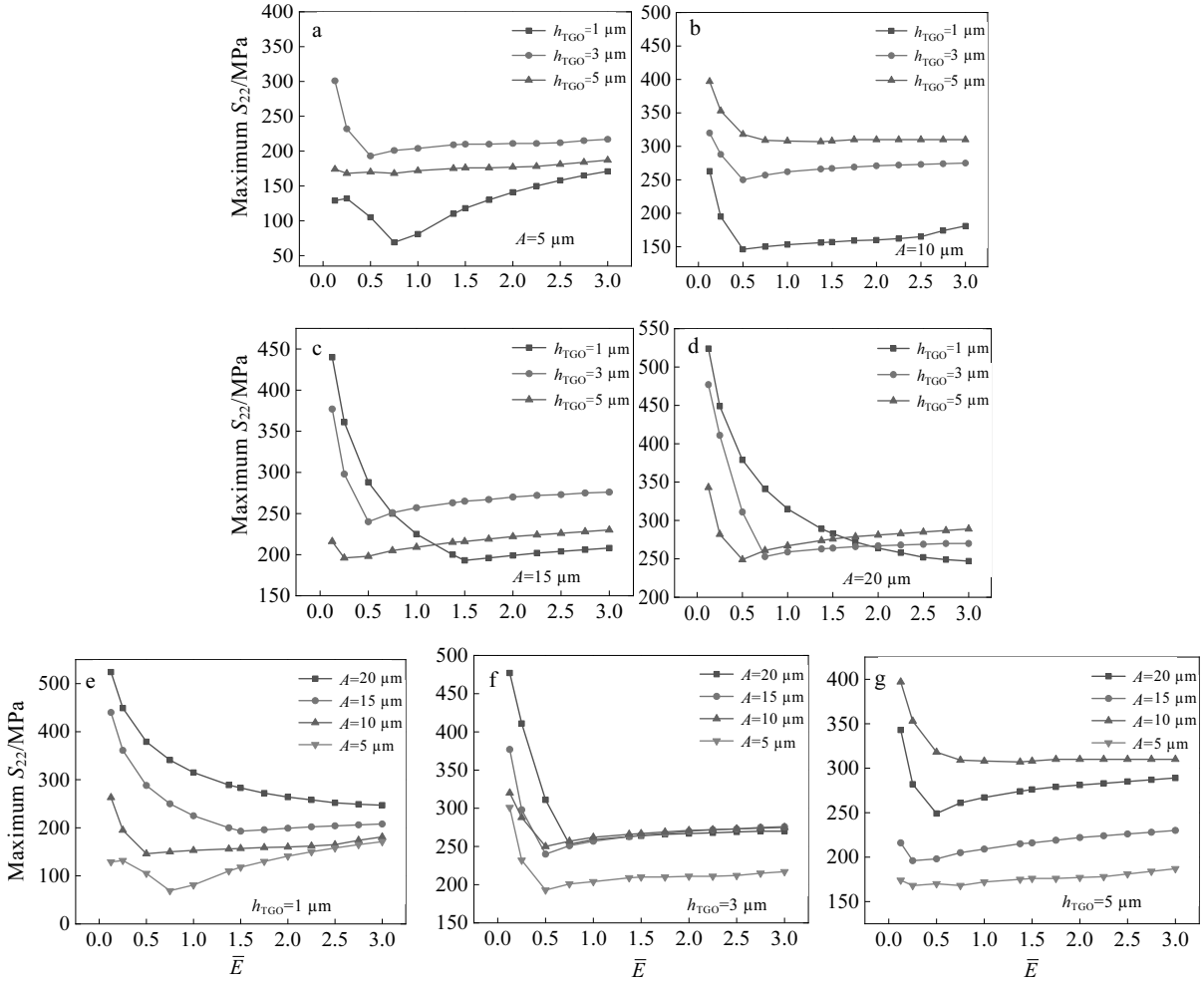

Fig.8 Effect of CMAS elastic modulus on maximum residual stress (S_{22}) in TC layer under the same TGO amplitudes and different TGO thicknesses (a~d) and the same TGO thicknesses and different TGO amplitudes (e~g)

modulus, but the increase is small. It can be considered that the maximum residual stress is basically not affected by the increase of the elastic modulus of CMAS.

When the TGO amplitude is 15 μm (Fig.8c), the TGO critical points under thicknesses of 5, 3, and 1 μm are around $\overline{E}=0.25$, $\overline{E}=0.5$, and $\overline{E}=1.5$, respectively. The trend before the critical point is the same as the previous analysis, that is, the maximum residual stress decreases with the increase of the CMAS elastic modulus. The decrease range for thicknesses 1, 3, and 5 μm is about 56%, 36%, and 9%, respectively. After the critical point, the maximum residual stress of the three curves increases with the increase of the CMAS elastic modulus, but the amplitude is very small. It can also be considered that it is not affected by the increase of the CMAS elastic modulus.

When the amplitude of TGO is 20 μm (Fig.8d), the critical points of TGO with thickness of 5, 3, and 1 μm are near $\overline{E}=0.5$, $\overline{E}=0.75$, and $\overline{E}=2$, respectively. Similarly, before the critical point, the maximum residual stress decreases with the increase of the CMAS elastic modulus; the curve of thicknesses 1, 3, and 5 μm decreases by about 50%, 47%, and 27%, respectively. After the critical point, the maximum residual stress of the three curves is not substantially affected by the increase in the CMAS elastic modulus, which agrees with the previous analysis.

Fig.8e~8g show the change of the maximum residual stress with the elastic modulus of CMAS when the thickness of TGO is constant and the amplitude is different. When h_{TGO}=1 μm, it can be seen from the figure that as the amplitude of TGO increases, the critical point of the maximum residual stress curve gradually moves backward, that is to say, the $\overline{E}$ causes the change of the curve trend become larger and larger.

In addition, it can be seen from the analysis of the curve trend that the residual stress curves of different TGO amplitudes show different trends with the increase of CMAS elastic modulus after the critical point, but when the CMAS elastic modulus increases to a certain value, the growth trend tends to be stable, that is, it is basically no longer affected by the increase of CMAS elastic modulus. When h_{TGO}=3 μm, it can be found that as the amplitude of TGO increases, the critical point position of the maximum residual stress curve gradually stabilizes around $\overline{E}=0.5$, and after the critical point, it is almost not affected by the increase of the elastic modulus of CMAS. The trend under h_{TGO}=5 μm is similar to the case of h_{TGO}=3 μm, that is, the critical point position of the maximum residual stress curve gradually stabilizes near $\overline{E}=0.5$, and after the critical point, it is not substantially affected by the increase in CMAS elastic modulus. The difference is that after the critical point, the maximum residual stress of the curve is obviously affected by the amplitude of TGO, and the residual stress curve under different amplitudes has a stepped distribution.

4 Conclusions

1) Under the same CMAS elastic modulus, the larger the thickness of TGO, the longer the BC-TGO interface crack; when the CMAS elastic modulus increases, the length of BC-TGO interface crack becomes shorter gradually, and the smaller the thickness of TGO, the greater the reduction of the interface crack length. It is indicated that the increase of elastic modulus of CMAS has an inhibitory effect on interfacial cracks. The smaller the thickness of TGO, the more obvious the inhibiting effect on the interfacial crack. Under the same CMAS elastic modulus, the larger the TGO amplitude, the longer the BC-TGO interface crack; when the CMAS elastic modulus increases, the BC-TGO interface crack length becomes shorter, and the smaller the amplitude of TGO, the greater the magnitude of the interface crack length reduction. It is shown that the increase of elastic modulus of CMAS can inhibit the interfacial crack, and the smaller the amplitude of TGO, the more obvious the inhibiting effect on the interfacial crack.

2) The influence of the change of CMAS elastic modulus on the maximum residual stress of TC layer has the following rules. First, there is a critical point for CMAS elastic modulus. Before the critical point, the change of elastic modulus of CMAS has a great influence on the maximum residual stress of TC layer, and with the increase of elastic modulus of CMAS, the maximum residual stress of TC layer decreases greatly. After the critical point, the maximum residual stress of TC layer is hardly affected by the change of CMAS elastic modulus. Second, it is found that the change of elastic modulus of CMAS has an obvious effect on the smaller thickness of TGO under different TGO amplitudes. On the one hand, when the thickness of TGO is smaller, the critical point of CMAS elastic modulus increases with the increase of the TGO amplitude. On the other hand, when the thickness of TGO is relatively small, for example, the thickness of TGO is 1 μm, after the critical point of CMAS elastic modulus, the maximum residual stress curve of TC layer becomes stable gradually after the increase of CMAS elastic modulus to a certain value. That is to say, compared with the thicker TGO, the maximum residual stress for thinner TGO is remarkably affected by CMAS elastic modulus. Thirdly, after the critical point, the maximum residual stress of the larger thickness of the TGO curve is obviously affected by the magnitude of the TGO, and the residual stress curves of different magnitudes show a stepped distribution.

References

1 Padture N P, Maurice G, Jordan E H. *Science*[J], 2002, 296(5566): 280

2 Vitor Emanuel de M L da S P, Nicholls J R, Newton R. *Surface and Coatings Technology*[J], 2017, 311: 307

3 Borom M P, Johnson C A, Peluso L A. *Surface & Coatings Technology*[J], 1996, 86-87(96): 116

4 Aygun A, Vasiliev A L, Padture N P *et al. Acta Materialia*[J], 2007, 55(20): 6734

5 Li L, Clarke D R. *International Journal of Applied Ceramic Technology*[J], 2010, 5(3): 278
6 Peng H, Wang L, Guo L *et al. Progress in Natural Science: Materials International*[J], 2012, 22(5): 461
7 Jing W, Guo H B, Gao Y Z. *Journal of the European Ceramic Society*[J], 2011, 31(10): 1881
8 Krämer S, Yang J, Levi C G. *Journal of the American Ceramic Society*[J], 2006, 89: 3167
9 Mercer C, Faulhaber S, Evans A G *et al. Acta Materialia*[J], 2005, 53(4): 1029
10 Su L, Chen X, Wang T J. *Surface and Coatings Technology*[J], 2015, 280: 100
11 Su L, Yi C. *Ceramics International*[J], 2017, 43(12): 8893
12 Li B, Fan X, Zhou K *et al. Ceramics International*[J], 2017, 43(17): 14 763
13 Fan X L, Zhang W X, Wang T J *et al. Surface and Coatings Technology*[J], 2012, 208: 7
14 Zhu W, Cai M, Yang L *et al. Surface & Coatings Technology*[J], 2015, 276: 160
15 Li B, Fan X, Zhou K *et al. International Journal of Mechanical Sciences*[J], 2018, 135: 31
16 Li S, Qi H, Song J *et al. Science China Technological Sciences*[J], 2019, 62(6): 989
17 Yu Q M, He Q, Ning F L. *Ceramics International*[J], 2018, 44(17): 21 349
18 Zhu W, Jin Y J, Yang L *et al. Wear*[J], 2018, 414-415: 303
19 Wellman R, Whitman G, Nicholls J R. *International Journal of Refractory Metals & Hard Materials*[J], 2010, 28(1): 124
20 Vidal-Setif M H, Chellah N, Rio C *et al. Surface & Coatings Technology*[J], 2012, 208(3): 39
21 Zhang G., Fan X, Xu R *et al. Ceramics International*[J], 2018, 44(11): 12 655
22 Hui Meiting, Yu Qingmin, Shi Yongzhi. *Ceramics International*[J], 2019, 45(7): 8414
23 Yu Q M, He Q. *Ceramics International*[J], 2018, 44(3): 3371
24 Lv B, Fan X, Li D *et al. Journal of the European Ceramic Society*[J], 2018. 38(4): 1946
25 Dassault SystemesSimulia Corp. *ABAQUS*, *Version 6.11 Documentation*[M]. Rhode Island: Dassault SystemesSimulia Corp, 2011
26 Turkdogan T E. *Physical Chemistry of High Temperature Technology*[M]. New York: Academic Press, 1980
27 Zhou Y C, Hashida T. *International Journal of Solids and Structures*[J], 2001, 38(24): 4235
28 Dongbo Z, Jian C, Jianjun Z. *Rare Metal Materials and Engineering*[J], 2012, 41: 505
29 Yu Q M, Zhou H L, Wang L B. *Ceramics International*[J], 2016, 42(7): 8338
30 Dugdale D S. *Journal of the Mechanics & Physics of Solids*[J], 1960, 8(2): 100
31 Barenblatt G I. *Advances in Applied Mechanics*[J], 1962, 7: 55
32 Jiang J, Wang W, Zhao X *et al. Engineering Fracture Mechanics*[J], 2018, 196: 191
33 Chandra N, Li H, Shet C *et al. International Journal of Solids and Structures*[J], 2002, 39(10): 2827
34 Zhu W, Yang L, Guo J W *et al. International Journal of Plasticity*[J], 2015, 64: 76
35 Xu W, Wei Y. *Computational Materials Science*[J], 2012, 53(1): 444
36 Camanho P P, Dávila C G, Moura M D. *Journal of Composite Materials*[J], 2003, 37(16): 1415
37 Mi Y, Crisfield M A, Davies G A O *et al. Delamination Behaviour of Composites*[J], 1998, 32(14): 367
38 Cen L, Qin W Y, Yu Q M. *Surface and Coatings Technology*[J], 2019, 358: 785
39 Białas M. *Surface and Coatings Technology*[J], 2008, 202(24): 6002
40 Xu T, He M Y, Evans A G. *Interface Science*[J], 2003, 11(3): 349
41 Mao W G, Wan J, Dai C Y. *Surface and Coatings Technology*[J], 2012, 206(21): 4455
42 Jiang J, Wang W, Zhao X *et al. Engineering Fracture Mechanics*[J], 2018, 196: 191

CMAS 对热障涂层界面裂纹和残余应力的影响

郭　盾，于庆民，岑　吕
(西北工业大学，陕西 西安 710129)

摘　要：随着航空发动机涡轮叶片工作温度的提升，一种主要由 CaO，MgO，Al_2O_3 和 SiO_2 组成的玻璃态物质（CMAS）对热障涂层的危害越来越严重，从而对热障涂层的性能和耐久性有了更高的要求。以电子束物理气相沉积热障涂层为研究对象，利用有限元方法研究了 CMAS 的渗入对界面裂纹扩展及陶瓷层（TC）内部残余应力的影响规律。采用波长固定、振幅变化的正弦曲线表示不同粗糙度的涂层界面，同时考虑了 CMAS 的弹性模量变化的影响及不同界面形貌与 CMAS 之间的相互作用。结果表明：CMAS 弹性模量的增加对界面裂纹具有抑制作用，并且热生长氧化层(TGO)幅值和厚度越小，抑制作用越明显。CMAS 弹性模量对 TC 层最大残余应力 S_{22} 的影响存在临界点，在临界点之前，CMAS 弹性模量的变化对 TC 层最大残余应力的影响较大，随着 CMAS 弹性模量的增加，TC 层最大残余应力大幅度减小；在临界点之后，TC 层最大残余应力基本不受 CMAS 弹性模量变化的影响。这些结果对电子束物理气相沉积喷涂的热障涂层失效机理的研究具有重要意义，可以为热障涂层界面的优化提供指导。

关键词：热障涂层；CMAS；界面形貌；有限元方法；内聚力模型

作者简介：郭　盾，男，1995 年生，硕士生，西北工业大学力学与土木建筑学院，陕西 西安 710129，电话：029-88431000，E-mail: Daer0601@163.com